Available online at www.sciencedirect.com

SCIENCE DIRECT®

International Journal of Pressure Vessels and Piping 81 (2004) 761–770

INTERNATIONAL JOURNAL OF
Pressure Vessels
and Piping

www.elsevier.com/locate/ijpvp

Structural integrity assessments of high pressure pipelines with axial flaws using a micromechanics model

Fernando Dotta, Claudio Ruggieri*

Department of Naval Architecture and Ocean Engineering, University of Sao Paulo, Av. Prof. Mello Moraes, 2231 (PNV-EPUSP),
São Paulo, SP 05508-900, Brazil

Received 10 December 2003; revised 30 April 2004; accepted 30 April 2004

Abstract

This study extends a micromechanics approach based upon the computational cell methodology to model ductile crack extension of longitudinal crack-like defects in a high strength pipeline steel. Laboratory testing of an API 5L X60 steel at room temperature using standard, deep crack $C(T)$ specimens provides the data needed to measure the crack growth resistance curve for the material. A simple scheme to calibrate material-specific parameters for the cells employs this measured R-curve. A central focus of the paper is the application of the cell methodology to predict experimentally measured burst pressures for longitudinally pre-cracked pipe specimens. The experimental program includes large-diameter pipe specimens with different crack depth (a) and crack size ($2c$). Plane-strain computations are conducted on detailed finite element models for the pipe specimens to describe crack extension with increased pressure. The cell model predictions of crack growth response and burst pressure predictions are in good agreement with experimental measurements for the tested pipes. The present methodology holds significant promise as an engineering tool to simulate ductile crack growth and to predict the burst pressure of high pressure pipelines containing crack-like defects.

Keywords: Axial flaws; Burst pressure; Pipeline steel; Ductile failure; Computational cell; Finite element analysis; Bulging effect

---

1. Introduction

The accurate prediction of the failure pressure in damaged pipelines remains a key issue for the safety assessment of high pressure piping systems, including onshore and offshore facilities. Conventional failure criteria for longitudinal crack-like defects in pipelines (e.g. blunt corrosion, inclusions, weld flaws, etc.) are derived based upon a simple fracture mechanics analysis for planar or crack-like flaws. Such procedures are calibrated by extensive burst testing of pipes containing machined cracks conducted on low-to-moderate strength structural steels (API Grades X52 and X60) [1–3]. While these acceptance criteria for linepipe defects clearly simplify integrity analyses of in-service piping components, they essentially reflect a limit-load solution for a blunted axial crack in a pressurized vessel or pipe. Moreover, these integrity assessment procedures assume failure criteria which do not necessarily reflect the actual failure mechanism (such as, for example, stable crack growth prior to final failure) nor do they address specific requirements for high grade pipe steels currently used. For these cases, failure assessments may be overly conservative or provide significant scatter in their predictions, which lead to unnecessary repair or replacement of in-service pipelines [4].

For high toughness pipeline steels, the material failure (leakage or sudden rupture) is most often preceded by large amounts of slow, stable crack growth. Under sustained ductile tearing of a macroscopic crack, large increases in the load-carrying (pressure) capacity for the flawed piping component are possible beyond the limits given by conventional elastic and elastic–plastic (stationary crack) analysis. Analytical methods for defect assessment in ductile materials generally employ the J-integral fracture parameter [5,6] to characterize the significant increase in toughness over the first few millimetres of stable crack extension (Δa). These methods rely on the direct application of crack growth resistance ($J-\Delta a$) curves (also often termed R-curves) measured using small, laboratory specimens to

---

* Corresponding author. Fax: +55-11-3091-5717.
E-mail address: claudio.ruggieri@poli.usp.br (C. Ruggieri).

0308-0161/$ - see front matter © 2004 Elsevier Ltd. All rights reserved.
doi:10.1016/j.ijpvp.2004.04.004

the surface defects in pressure vessels and pipelines [7–9]. However, laboratory testing of fracture specimens to measure resistance curves consistently reveals a marked effect of absolute specimen size, geometry, relative crack size (a/W) and loading mode (tension vs. bending) on R-curves. For the same material, deep-notch bend, SE(B), and compact tension, $C(T)$, specimens yield low R-curves while shallow-notch SE(B), single-edge notch tension, SE(T), and middle-crack tension, $M(T)$, specimens yield larger toughness values at similar amounts of crack extension (see Refs. [10,11] for illustrative examples). These effects observed in R-curves arise from the strong interaction between microstructural features of the material which govern the actual separation process and the loss of stress triaxiality in the crack front region due to large-scale yielding. Consequently, advanced methodologies for fracture assessments of pipelines must include robust procedures to transfer fracture resistance data measured using small laboratory specimens to structural piping components in engineering applications.

The above arguments underly the key role played by ductile tearing predictions in structural integrity assessments of pipelines using crack growth resistance data. Current engineering approaches to describe stable crack extension in ductile materials employ micromechanics models which couple macroscale features of crack growth with the dominant microscale damage of common pressure vessel and pipeline steels, such as void nucleation, growth and coalescence. In particular, the cell methodology proposed by Xia and Shih [12] and extended in a 3D context by Ruggieri et al. [13] and Gullerud et al. [14] provides a computational model which links the macroscopic fracture resistance ($J-\Delta a$) to these microstructural features and the flow properties for the material. Computational cell elements defined over a thin layer of material ahead of the crack tip provide the physical model to describe ductile crack extension under Mode I loading. Within each cell, void growth and material softening are modeled by the Gurson–Tvergaard (GT) dilatant plasticity theory [15,16]; ductile crack extension occurs through cell extinction within this thin layer of material ahead of the crack tip. The cell size represents roughly the mean spacing of the larger, void initiating inclusions such as MnS particles typically found in common pressure vessel and pipeline steels. Numerical analyses of fracture specimens using the cell model have predicted the effects of geometry on R-curves and measured crack front profiles with surprising accuracy [13].

This study extends a micromechanics approach based upon the computational cell methodology to model ductile crack extension of longitudinal crack-like defects in a high strength pipeline steel. The first section outlines the main features of the cell modeling strategy to describe Mode I crack growth in ductile materials. Laboratory testing of an API 5L X60 steel at room temperature using standard, deep crack $C(T)$ specimens provides the data needed to measure the crack growth resistance curve for the material. A simple scheme to calibrate material-specific parameters for the cells employs this measured R-curve. A central focus of the paper is the application of the cell methodology to predict experimentally measured burst pressures for pipe specimens with axial crack-like flaws. The experimental program includes large-diameter pipe specimens with different crack depth (a) and crack size ($2c$). Plane-strain computations are conducted on detailed finite element models for the pipe specimens to describe crack extension with increased pressure. The cell model predictions of crack growth response and burst pressure predictions are in good agreement with experimental measurements for the tested pipes. The present methodology holds significant promise as an engineering tool to simulate ductile crack growth and to predict the burst pressure of pipes and pressure vessels containing crack-like defects.

2. Overview of micromechanics modeling for ductile tearing

Ductile fracture in metals is a multistep mode of material failure incorporating the combination of microvoid nucleation, growth and coalescence at the microscale level (see, e.g. the review of Garrison and Moody [17]). Microvoids nucleate at inclusions or second-phase particles, either by decohesion of the particle–matrix interface or by fracture of the particles. Under increased deformation, these microvoids grow until localized plastic flow and necking of the ligament between adjacent microvoids (coalescence of microvoids) create a continuous fracture path (most often assisted by the rapid growth and coalescence of secondary microvoids). Experimental observations and computational studies enable simplification of the detailed microregime of failure described above by assuming the growth of microvoids as the critical event controlling ductile extension. Fig. 1(a) pictures the schematic path of a Mode I growing crack in a ductile material. The material layer enveloping the growing crack, which must be thick enough to include at least a void or microcrack nucleus, identifies

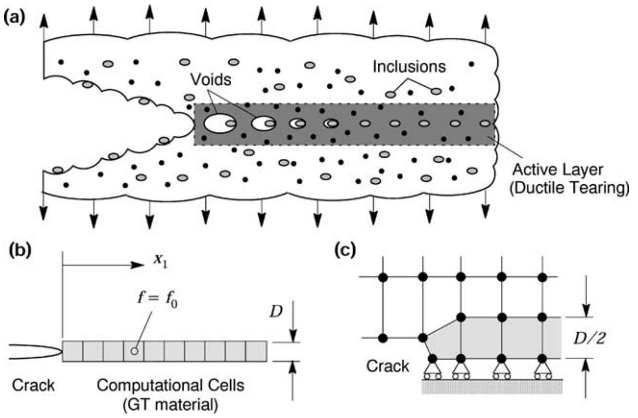

Fig. 1. Model for ductile crack growth using computational cells [13].

a process zone for the ductile fracture which conveniently gives the necessary length dimension for the model. Void growth and coalescence in the layer will cause the surface tractions that the process zone exerts on its surrounding to drop to zero thereby advancing the physical crack.

Motivated by the above observations, Xia and Shih [12] proposed a model using computational cells to include a realistic void growth mechanism, and a microstructural length-scale physically coupled to the size of the fracture process zone. Void growth remains confined to a layer of material symmetrically located about the crack plane, as illustrated in Fig. 1(b), and having thickness D, where D is associated with the mean spacing of the larger, void initiating inclusions. This layer consists of cubical cell elements with dimension D; each cell contains a cavity of initial volume fraction f_0 (the initial void volume divided by cell volume). Fig. 1(c) displays the finite element implementation of the cell model thereby defining the computational cells. Material outside these computational cells, the 'background' material, follows a conventional J_2 flow theory of plasticity and remains undamaged by void growth in the cells. As a further simplification, the void nucleates from an inclusion of relative size f_0 immediately upon loading. Progressive void growth and subsequent macroscopic material softening in each cell are described with the Gurson–Tvergaard (GT) constitutive model for dilatant plasticity [15,16] given by

$$g(\sigma_e, \sigma_m, \bar{\sigma}, f) = \left(\frac{\sigma_e}{\bar{\sigma}}\right)^2 + 2q_1 f \cosh\left(\frac{3q_2\sigma_m}{2\bar{\sigma}}\right) - (1 + q_3 f^2) = 0 \qquad (1)$$

where σ_e denotes the effective Mises (macroscopic) stress, σ_m is the mean (macroscopic) stress, $\bar{\sigma}$ is the current flow stress of the cell matrix material and f defines the current void fraction. Under multiaxial stress states, $\sigma_e = (3S_{ij}S_{ij}/2)^{1/2}$ where S_{ij} denotes the deviatoric components of Cauchy stress. Factors, q_1, q_2 and $q_3 = q_1^2$ introduced by Tvergaard improve the model predictions for periodic arrays of cylindrical and spherical voids. Faleskog et al. [18] conducted a series of numerical analyses to determine values of q_1 and q_2 for varying material flow properties. Following their work, we use $q_1 = 1.43$ and $q_2 = 0.83$.

The GT yield function in Eq. (1) does not model realistically the rapid loss of stress capacity for larger void fractions nearing coalescence levels, nor does the model create new traction free surfaces to represent physical crack extension. In the present work, the evolution of stress within cells follows the original constitutive model of GT in Eq. (1) until $f = f_E$. The final stage of void link-up with the macroscopic crack front then occurs by reducing the remaining stresses to zero in a prescribed manner. Tvergaard [16] refers to this process as the element extinction or vanish technique. The cell extinction process implements a linear-traction separation model (see additional details in Ref. [13]). When f in the cell incident on the current crack tip reaches a critical value, f_E, the computational procedures remove the cell thereby advancing the crack tip in discrete increments of the cell size. Previous analyses [12,13] and experimental observations indicate a value of f_E between 0.15 and 0.25; such a range of f_E-values does not alter the extinction process nor the crack advance in the numerical model for large volume fractions ($f > 0.15$). Here, we adopt $f_E = 0.2$.

3. Experimental measurements

To investigate the failure behaviour of axially flawed pipelines, a series of full scale burst tests were performed on end-capped pipe specimens with external diameter, $D_e = 508$ mm, wall thickness, $t = 15.8$ mm and length, $L = 3$ m [19]. These experimental tests are part of a pipeline integrity program conducted by the Brazilian State Oil Company (Petrobrás) and included both internal and external longitudinal surface cracks with different sizes measured by crack depth and crack length, $a \times 2c$, with a fixed $a/2c$-ratio of 0.05. The present work considers pipe specimens with 7×140 mm and 10×200 mm longitudinal flaws; hereafter, these pipe configurations are simply denoted as 7 and 10 mm cracked pipes. Fig. 2(a) provides a schematic illustration of the pipe specimen with an external longitudinal flaw. These specimens were notched along their length using an electrical discharge machine (EDM) to create the required notch shape. The initial semi-elliptical defects were not subjected to a pressure cycle to propagate a fatigue crack from the original notch. However, the high accurate machining process allows considering them as initially blunted cracks. During the loading of the pipes, ductile crack extension was monitored by using an ultrasonic pulse technique to measure the crack growth at the deepest point of the surface defect [20].

The material is an API 5L Grade X60 [22] pipeline steel with 483 MPa yield stress (σ_{ys}) at room temperature (20 °C) and relatively low hardening properties ($\sigma_u/\sigma_{ys} \approx 1.24$), where σ_u is the ultimate tensile strength. Table 1 lists

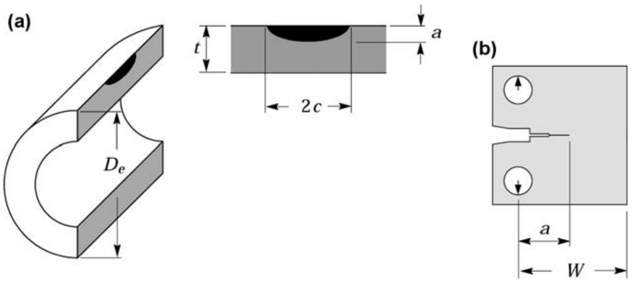

Fig. 2. (a) Pipe specimen with external crack employed in the burst tests. (b) Standard deep notch $C(T)$ specimen utilized to determine the crack growth resistance curve for the tested pipeline steel.

Table 1
Chemical composition of tested API 5L X60 steel (mass%) [21]

C	Si	Mn	P	S	Cu	Ni
0.12	0.29	1.42	0.021	0.009	0.01	0.02
Cr	Mo	Nb	V	Al	Ti	B
0.02	0.01	0.026	0.04	0.023	0.01	0.007

the chemical composition of this material. Rectangular tensile specimens (ASTM A370) [23] with 13 mm thickness were extracted from the circumferential orientation of the pipe (which is also the transverse direction of the steel plate) to provide the mechanical properties at room temperature [21]. Table 2 summarizes the mechanical properties obtained from these tests. Fig. 3 displays the engineering stress–strain data for this pipeline steel obtained using the rectangular specimens (average of three tensile tests). Other mechanical properties for the material include Young's modulus, $E = 210$ GPa and Poisson's ratio, $\nu = 0.3$.

Laboratory testing of standard compact tension $C(T)$ specimens (side-grooved) extracted from the pipe in the TL position provided the tearing resistance curves (J vs. Δa) at room temperature (20 °C) to calibrate the cell parameters for the tested pipeline steel [24]. These fracture specimens have thickness $B = 13$ mm (0.5-T) and width $W = 26$ mm with crack length, a, to width ratio, $a/W = 0.5$ (refer to Fig. 2(b)). After fatigue pre-cracking, the specimens were side-grooved to a depth of 1 mm on each side to promote uniform crack growth over the thickness. The 0.5-T $C(T)$ specimens were tested at room temperature using a direct current potential (DCP) method to measure the crack growth resistance for the material. The fracture tests followed the procedures of ASTM Standard Test Method for Measurement of Fracture Toughness and R Curves (E1820). Experimental J-values are determined using the measured load–load line displacement records. Fig. 4 presents the experimentally measured J vs. Δa curves; a simple extrapolation procedure indicates a value of J at initiation of ductile tearing, $J_{Ic} \approx 207$ kJ/m^2 [24]. While the experimental data for high values of ductile tearing ($\Delta a \gtrsim 2.5$ mm) are somewhat beyond the limits given by ASTM E1820, these measured R-curves are used in a phenomenological manner (see Section 5) in that they are essentially employed to calibrate the micromechanics parameters D and f_0 and not the toughness capacity of the fracture specimen.

Table 2
Mechanical properties of tested API 5L X60 steel at room temperature [21]

σ_{ys} (MPa)	σ_u (MPa)	ε_t (%)	σ_u/σ_{ys}
483	597	29	1.24

σ_{ys}, 0.2% proof stress; σ_u, ultimate tensile strength; ε_t, uniform elongation (gauge length = 50 mm).

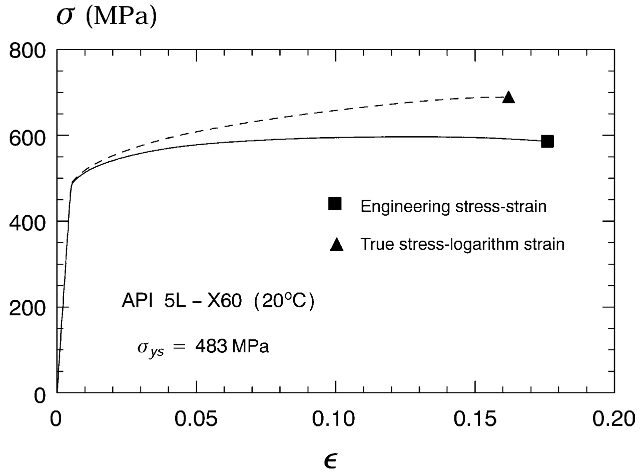

Fig. 3. Uniaxial stress–strain response of API 5L X60 steel employed in the analyses.

4. Finite element procedures

Nonlinear finite element analyses are performed on plane-strain models for the side-grooved $C(T)$ specimen and the longitudinally pre-cracked pipe specimens. The numerical computations for the crack growth analyses reported here are generated using the research code WARP3D [25]. Key features of the code employed in this work include: (1) the GT and Mises constitutive models implemented in a finite-strain setting, (2) cell extinction using a linear traction-separation model, (3) automatic load step sizing based on the rate of damage accumulation, and (4) evaluation of the J-integral using a domain integral procedure [26]. WARP3D analyzes fracture models constructed with 3D, eight-node trilinear hexahedral elements. To achieve plane-strain conditions for the current study, a single thickness layer of the 3D elements is defined with out-of-plane displacements constrained to vanish.

A piecewise-linear approximation of the measured engineering stress–strain curve for the API X60 steel

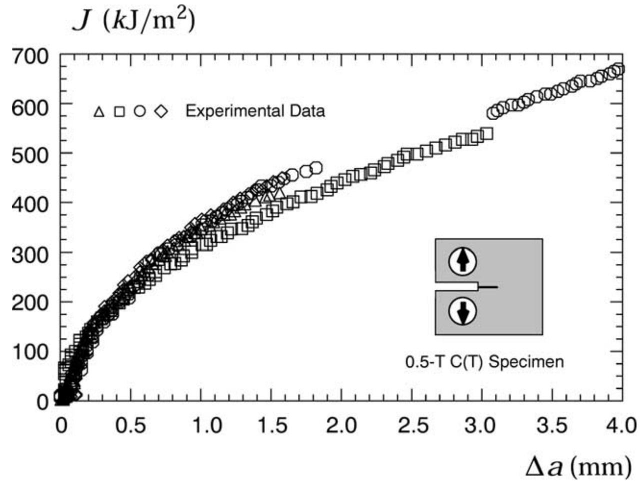

Fig. 4. Experimental J-resistance curves of the tested API 5L X60 steel for the 0.5-T $C(T)$ specimens [24].

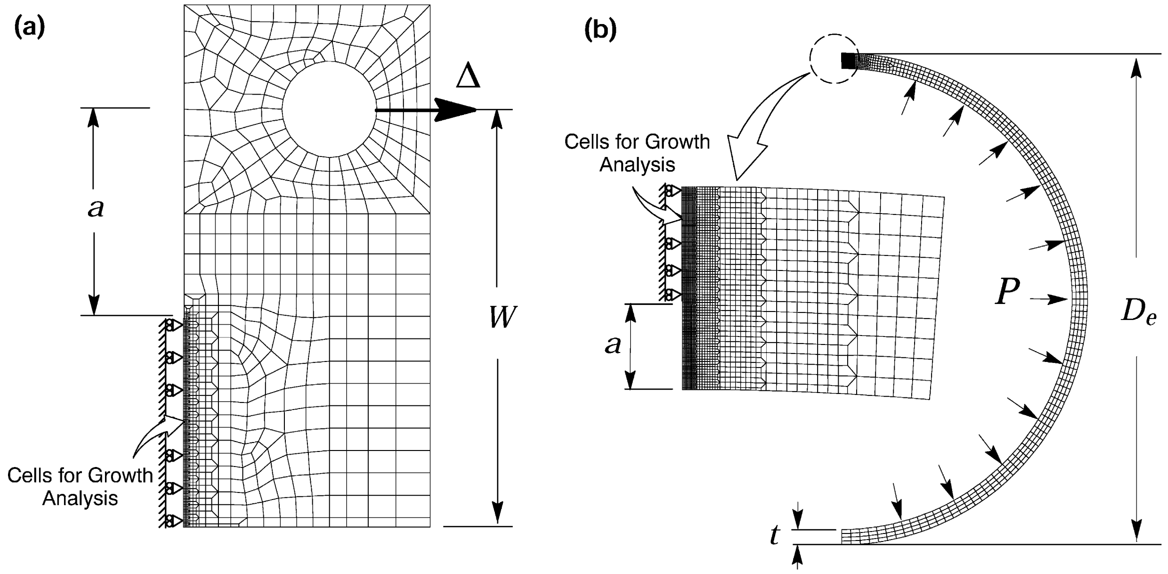

Fig. 5. Plane-strain finite element models used in crack growth analyses: (a) 0.5-T $C(T)$ specimen, (b) Pipe specimen ($D_e = 508$ mm) with 7 × 140 mm internal crack.

shown in Fig. 3 is adopted to generate numerical solutions for the fracture and pipe specimens described in Section 5. The material has a Young's modulus $E = 210$ GPa, Poisson's ration $\nu = 0.3$ and yield stress $\sigma_{ys} = 483$ MPa at room temperature (20 °C). The matrix material of the computational cell elements and the void-free background material are assigned these properties.

Fig. 5(a) shows the finite element model constructed for the plane-strain analyses of the 0.5-T $C(T)$ specimen ($B = 13$ mm) with $a/W = 0.5$. Symmetry conditions permit modeling of only one-half of the specimen with appropriate constraints imposed on the remaining ligament. The half-symmetric model has one thickness layer of 1078 eight-node, 3D elements with plane-strain constraints imposed ($w = 0$) on each node. Displacement controlled loading applied at the pin hole indicated in Fig. 5(a) enables continuation of the analyses once the load decreases during crack growth. To simulate ductile crack extension, the finite element mesh contains a row of 130 computational cells along the remaining crack ligament ($W - a$) in a similar arrangement as shown in Fig. 1(b) and (c). The initially blunted crack tip accommodates the intense plastic deformation and initiation of stable crack growth in the early part of ductile tearing.

Plane-strain finite element analyses are also conducted on the longitudinally cracked pipes with 7 and 10 mm cracks (both internal and external). Fig. 5(b) shows the finite element model constructed for the 7 mm cracked pipe specimen with an internal flaw. The half-symmetric model has one thickness layer of 3497 eight-node, 3D elements with plane-strain constraints ($w = 0$) imposed on each node. Here, the finite element mesh contains a row of 88 computational cells along the remaining crack ligament ($t - a$). Very similar finite element models and mesh configurations are employed for other pre-cracked pipe configurations. The numerical analyses for the pipes with internal cracks also considered crack face loading due to internal pressure.

5. Numerical simulation of ductile tearing

5.1. Micromechanics calibration of cell parameters

The cell size D and initial porosity f_0 define the key *micromechanics* parameters coupling the physical and computational models for ductile tearing. To apply the cell model to a specific material, these two parameters must be *calibrated* to bring the numerical predictions into agreement with experimental measurements. These parameters should not be viewed as metallurgical parameters representing the microscopic observations of void spacing and initial void volume fraction but rather as *computational* parameters phenomenologically calibrated. Here, we choose the cell parameters D and f_0 which provide the best fit to the experimentally measured R-curves (see Fig. 4) for the material. The calibrated values for these parameters are then applied in numerical analyses with similar mesh details to predict ductile extension in the pre-cracked pipe specimens.

The approximate correlation of spacing between the large inclusions and the crack tip opening displacement (CTOD) at the onset of macroscopic crack growth in conventional fracture specimens for common pressure vessel steels provides values for D in the 50–200 μm range [12,13,27]. Such a range of values should also be applicable to the modeling of ductile failure behaviour in a pipeline steel using the computational cells. While the mapping of one finite element per cell must provide adequate resolution of the stress–strain fields in the active layer and in the adjacent background material, the numerical crack growth response of the $C(T)$ specimen scales almost proportionally with D for fixed f_0 (a thicker layer requires more total work to reach critical conditions). Consequently, the calibrated values for D and f_0 clearly do not constitute a unique pair of parameters; for example, a slightly larger D value may be compensated for by a larger f_0-value. Nevertheless, there exists a reasonably narrow range of D and f_0 pairs which yield the numerical R-curve in agreement with the experimental results. Guided by previous plane-strain analyses [13] and experimental observations, we specified the cell size $D/2 = 100$ μm for the API X60 material employed in this study. With the length scale, D, fixed for the numerical analyses, the calibration process then focuses on determining a suitable value for the initial volume fraction, f_0, that produces the best fit to the measured crack growth data for the deeply cracked specimens. Because each change in D requires construction of a new mesh, it is obviously much less effort to fix D early on and then calibrate f_0.

Fig. 6 shows the measured (open symbols) and predicted J–Δa curves for the 0.5-T $C(T)$ specimen. Predicted R-curves are shown for three values of the initial volume fraction, $f_0 = 0.006$, 0.007 and 0.008. For consistency, the location of the growing crack tip in the analysis is taken at the cell with $f = 0.1$. As demonstrated by Ruggieri and Dodds [13], this corresponds to a position between the cell currently undergoing extinction and the peak stress location; at this position stresses are decreasing rapidly and the void fraction is increasing sharply. Consequently, the use of slightly different f values, other than 0.1, to define the crack-tip location for plotting purposes does not appreciably alter the R-curves (at a fixed J, the amount of crack extension would vary only by a fraction of the cell size). For $f_0 = 0.008$, the predicted R-curve agrees well with the measured values for almost the entire crack extension range; for $\Delta a \gtrsim 2$ mm the predicted curve lies a little above the measured data. In contrast, the use of $f_0 = 0.007$ and 0.006 produces a much higher resistance curve relative to the measured data. Consequently, the initial volume fraction $f_0 = 0.008$ is taken as the calibrated value for the API 5L-X60 steel used in the present study.

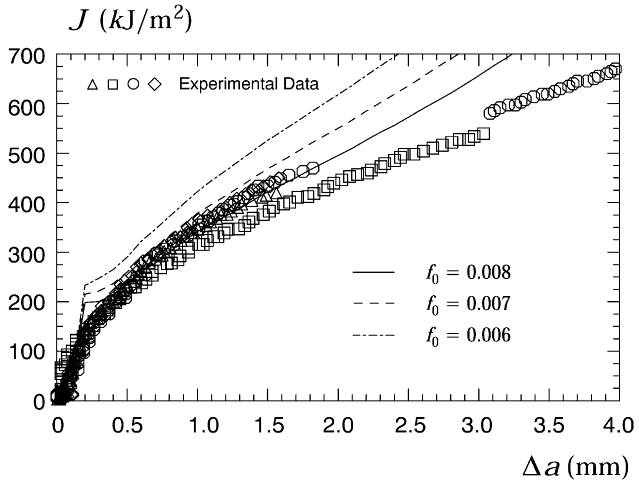

Fig. 6. Predicted J-resistance curves of the tested API 5L X60 steel using the 0.5-T $C(T)$ specimens.

5.2. Numerical analyses of pipe specimens

The numerical analyses for the pipe specimens based upon the cell model employ plane-strain finite element computations as previously described. Figs. 7 and 8 present key results obtained from numerical simulations of the ductile behaviour for the pipe specimens using the cell model with $f_0 = 0.008$ and $D = 200$ μm. These parameters were calibrated for the 0.5-T $C(T)$ specimens and are adopted as the material-specific parameters in the present analyses. The results provide valuable insight into the relation between the dominant failure mode of the pipes and the local conditions near the crack tip based upon the cell analyses.

Fig. 7 displays the predicted evolution of crack growth with increased internal pressure for the analyzed pipe specimens. To provide a simple comparison with the experimental data, this plot also includes the measured crack extension with increasing pressure for the pipe specimen with a 7 mm internal crack which was obtained using an ultrasonic pulse technique [20]. The general trend of crack growth evolution with increased pressure is correctly predicted for this pipe specimen. Unfortunately, the comparisons of numerical predictions with experimental data for other pipe specimens cannot be made here as the amount of ductile tearing was monitored only for one pipe specimen. Here, we note that the numerical predictions provide slightly lower pressure values for a fixed amount of crack growth. Such behaviour is most likely associated with discrepancies between the (numerical) elastic–plastic hardening model and the actual hardening behaviour for the material at higher strains. Moreover, the plane-strain

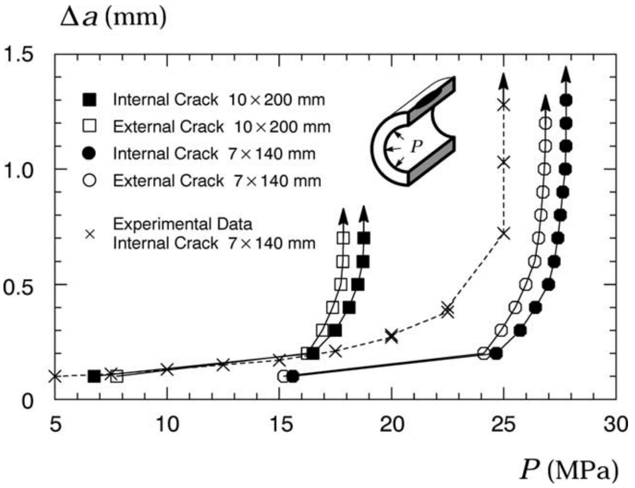

Fig. 7. Predicted evolution of crack growth with increased pressure for the pipe specimens using $f_0 = 0.008$ and comparison with experimental data for the pipe specimen with 7 × 140 mm internal crack.

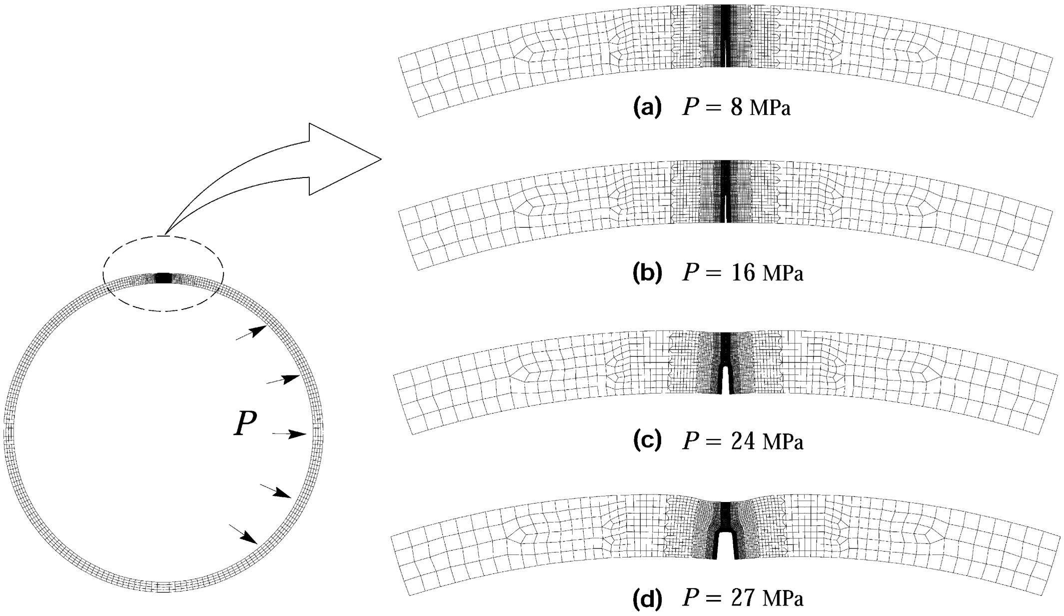

Fig. 8. Predicted evolution of bulging and crack opening for the pipe specimen with 7 × 140 mm internal crack at varying load (pressure) levels: (a) $P = 8$ MPa; (b) $P = 16$ MPa; (c) $P = 24$ MPa and (d) $P = 27$ MPa.

analyses of the pre-cracked pipe specimens represent an idealization of the actual pipe geometry; here, the surface cracks are viewed as infinite longitudinal (planar) cracks which cannot capture the (surface) crack front profile. Since only little crack extension occurs near the free surface of the crack, where plastic constraint remains low over the deformation history, the amount of ductile crack extension at the deepest point of the surface crack is clearly different from the corresponding crack extension for the plane strain crack. Nevertheless, the analyses clearly show increased pressure values with very little crack growth up to ~90% of the maximum pressure attained in the numerical simulations. After this pressure level, the region of damaged material ahead of the crack tip increases very rapidly thereby causing a significant crack extension just before final failure. When an instability point is eventually reached (points marked by arrows in Fig. 7), the remaining material in the crack ligament (defined by $t - a$ see Fig. 2) cannot keep pace with the increased pressure so that pipe collapse occurs.

Fig. 8(a)–(d) show the deformed profile for different load (pressure) levels, $P = 8$, 16, 24 and 27 MPa for the pipe specimen with a 7 mm internal crack. The pressure value $P = 27$ MPa marks the load almost immediately prior to pipe collapse (see Fig. 7). The predicted ductile behaviour reproduces the essential features of the inward deflection (bulging) mechanism in the damaged (cracked) region of the pipe as the pressure increases. Moreover, these plots aid in understanding the behaviour displayed in the previous Fig. 7 where there is a rapid increase in crack growth, Δa, for small changes in the internal pressure near the attainment of the maximum pressure in the experiments. Note the substantial change in the crack opening profiles for $P = 24$ and 27 MPa in comparison with the lower pressure levels. Following a transient period when the crack mouth opening remains relatively contained, the rapid development of the inward deflection (bulging) affects rather strongly the crack mouth opening and the amount of crack extension. The numerical results reported here for the pipe specimen with the 7 mm internal crack are essentially similar to corresponding results for other pipe specimens (to conserve space, they are not shown here).

6. Prediction of failure pressure for the pre-cracked pipes

6.1. Conventional failure criterion for axial blunt flaws

This section provides a simple comparison of the present methodology with a widely used acceptance criterion for axial blunt flaws in pipes and piping components. The approach is essentially derived from a limit-load solution for an elastic–plastic fracture mechanics analysis of a planar flaw [2]. A well-known expression for the failure (burst) pressure, P_B, for axially surface flawed pipes (see, for example, ASME Code Section XI [3]) is given by

$$P_B = \frac{t}{R_m}\left[\frac{1 - a/t}{1 - a/(tM_S)}\right]\sigma_f \tag{2}$$

with

$$M_S = \left(1 + 1.61\frac{c^2}{R_m t}\right)^{1/2} \tag{3}$$

where σ_f is the flow stress; a, the flaw depth; c, the half flaw length; t, the pipe wall thickness; R_m is the pipe mean radius.

Eq. (3) defines the bulging factor, M_S, for axial surface cracks developed by Kiefner et al. [2] which equates the crack driving force in a plate and the crack driving force for a pipe, both with the same crack size and at the same load level. The flow stress is most often evaluated as the simple average between the yield and tensile stress given by $(\sigma_{ys} + \sigma_u)/2$.

6.2. Burst pressure predictions using the micromechanics model

To verify the predictive capability of the micromechanics methodology adopted in the present work, this section describes a simple procedure to predict the measured burst pressure for the longitudinally cracked pipes based upon the cell model. The numerical predictions based upon the cell model employ plane-strain finite element analyses of these specimens using the cell parameters previously calibrated ($D = 200$ mm and $f_0 = 0.008$) for the 0.5-T $C(T)$ specimens. As already hinted before, the plane-strain idealization of the pipe specimen should provide a credible numerical model since the surface crack for all analyzed cases is relatively shallow and long ($a/2c = 0.05$).

Fig. 9 recasts the predicted ductile crack extension with internal pressure, P, presented previously (see Fig. 7) in terms of crack growth rate, here defined as the instantaneous variation of crack extension with pressure, da/dP, vs. increased applied pressure (P). Under increased internal pressure, the rate of crack growth increases very slowly up to $P \approx 18$ MPa for the pipe specimen with a 10 mm crack and $P \approx 26$ MPa for the pipe specimen with a 7 mm crack. These pressure values mark the beginning of very rapid ductile tearing with little increase in the applied pressure. After these pressure values (which are near the attainment of the maximum pressure observed in the tests), the load-carrying capacity of the remaining ligament cannot keep pace with the damage accumulation in the near-tip process zone (as characterized by the large number of damaged cell elements in the numerical model) so that an instability point is reached.

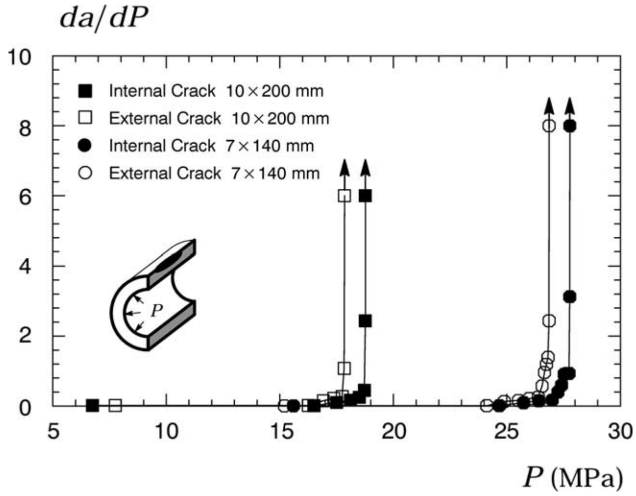

Fig. 9. Evolution of crack growth rate with increased pressure for the pipe specimens using $f_0 = 0.008$.

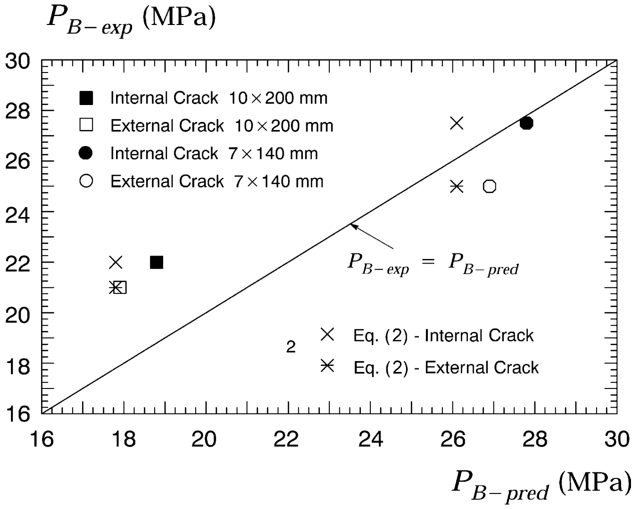

Fig. 10. Comparison between predicted and experimental burst pressures for the tested pipes.

Fig. 10 provides the predicted burst pressure for the tested pipes using the cell model. The symbols in the plots represent the predicted values whereas the solid line defines equality between the experiments and predictions, i.e. $P_{\text{B-exp}} = P_{\text{B-pred}}$. The plot also includes the predicted pressure values for the pipes using Eq. (2); here, the marks represent the predicted values. Table 3 compares the predicted burst pressures with the experimentally measured values. While the analyses yield failure (burst) pressure values which overall differ by less than 10% of the experimental values, predictions for the cell model show better agreement with experiments. In particular, analyses for the pipe specimens with an internal crack (solid symbols) provide good agreement with experiments. More importantly, however, the cell model has the capability to better capture the differences in measured failure pressures for the internal and external longitudinal cracks.

Table 3
Comparisons of measured and predicted burst pressures for the pipe specimens

$a \times 2c$ (mm)	a/t	Internal crack		External crack		Eq. (2)
		$P_{\text{B-exp}}$ (MPa)	$P_{\text{B-pred}}$ (MPa)	$P_{\text{B-exp}}$ (MPa)	$P_{\text{B-pred}}$ (MPa)	$P_{\text{B-pred}}$ (MPa)
7 × 140	0.44	7.5	27.8	25.0	26.9	26.0
10 × 200	0.63	22.0	18.8	21.0	17.9	17.8

7. Concluding remarks

This study reports an exploratory application of the computational cell model to analyze the ductile fracture behaviour of a high strength, pipeline steel (API Grade 5L X60). Laboratory testing of a deep crack, compact tension specimen provides the tearing resistance characteristics of the material which is used to calibrate the material-specific parameter f_0. The model accurately reproduces the evolution of crack growth (Δa) with increasing loading, as measured by the J-integral, for this specimen. The cell model incorporating the calibrated cell parameters is then applied to predict the burst pressure of a thin-walled pipeline containing surface crack-like flaws with different crack depth and crack length. The plane-strain analyses reported here demonstrate the capability of the computational cell approach to simulate ductile crack growth and to correctly predict the burst pressure for the pre-cracked pipe specimens containing relatively shallow and long cracks ($a/2c$-ratio of 0.05).

While the present study has not explored other ranges of crack configurations, pipe diameters/wall thickness and other material properties, the results presented here represent a compelling support to the predictive capability of the cell model. Moreover, application of the cell methodology within the framework of plane-strain models provides a relatively simple procedure to include ductile tearing effects in burst pressure predictions of cracked pipelines—the 1000–1500 element models with extensive ductile crack growth consume at most 1–2 h of time on a desktop PC.

Ongoing work with the computational cell framework focuses on modeling of ductile tearing in a full 3D setting for cracked pipelines. Specifically, differences in crack-tip constraint for the plane-strain model and the 3D model are currently being investigated. These studies can clarify whether the behaviour of the cell model and void growth response under conditions of varying stress triaxiality influences the amount of crack growth at fixed levels of remote loading (as measured by the internal pressure in the present analyses). Preliminary efforts along these lines reveal that very long and shallow axial flaws (such as, for example, blunt corrosion flaws along longitudinal welds in pipes) display crack growth behaviour which contrasts sharply with the corresponding behaviour of shorter and deeper axial flaws at the same load (pressure) level. Nevertheless, while the preliminary results reported here underlie the need for additional work to fully validate the cell model, the overall agreement between these less costly plane-strain analyses and experiments encourages further development of the present methodology as an engineering tool for failure assessments of damaged pipelines.

Acknowledgements

This investigation is supported by the State of São Paulo Research Foundation (FAPESP) through Grant 03/02735-6. The authors acknowledge the Brazilian State Oil Company (Petrobrás) for making available the experimental data for the API 5L X60 pipeline steel plate and the burst pressure data. The authors also acknowledge the many useful discussions and contributions of José Claudio Guimarães Teixeira and Eduardo Hippert Jr (CENPES-Petrobrás).

References

[1] The American Society of Mechanical Engineers. Manual for determining the remaining strength of corroded pipelines. ASME B31-G, New York; 1984.

[2] Kiefner JF, Maxey WA, Eiber RJ, Duffy AR. Failure stress levels of flaws in pressurized cylinders. Progress in flaw growth and fracture toughness testing. ASTM STP 536, Philadelphia, PA: American Society for Testing and Materials; 1973. p. 461–81.

[3] The American Society of Mechanical Engineers. Boiler and pressure vessel code, section XI. 1998.

[4] Wilkowski G, Stephens G, Krishnaswamy P, Leis B, Rudland D. Progress in development of acceptance criteria for local thinned areas in pipe and piping components. Nucl Eng Des 2000;(195):149–69.

[5] Hutchinson JW. Fundamentals of the phenomenological theory of nonlinear fracture mechanics. J Appl Mech 1983;(50):1042–51.

[6] Anderson TL. Fracture mechanics: fundaments and applications, 2nd ed. New York: CRC Press; 1995.

[7] Anderson TL, Gordon JR, Garwood SJ. On the application of R-curves and maximum load toughness to structures. Fracture Mechanics: Nineteenth Symposium. ASTM STP 969, Philadelphia, PA: American Society for Testing and Materials; 1988. p. 291–317.

[8] American Petroleum Institute. Recommended practice for fitness-for-service. API RP-579; 2000.

[9] British Standard Institution. Guide on methods for assessing the acceptability of flaws in metallic structures. BS7910; 1999.

[10] Hancock JW, Reuter WG, Parks DM. Constraint and toughness parameterized by T. Constraint effects in fracture. ASTM STP 1171, Philadelphia, PA: American Society for Testing and Materials; 1993. p. 21–40.

[11] Joyce JA, Link RE. Effects of constraint on upper-shelf fracture toughness. Fracture mechanics. ASTM STP 1256, vol. 26. Philadelphia, PA: American Society for Testing and Materials; 1995. p. 142–77.

[12] Xia L, Shih CF. Ductile crack growth. I. A numerical study using computational cells with microstructurally-based length scales. J Mech Phys Solids 1995;(43):233–59.

[13] Ruggieri C, Panontin TL, Dodds RH. Numerical modeling of ductile crack growth in 3-D using computational cells. Int J Fract 1996;(82): 67–95.

[14] Gullerud AS, Gao X, Dodds RH, Haj-Ali R. Simulation of ductile crack growth using computational cells: numerical aspects. Eng Fract Mech 2000;(66):65–92.

[15] Gurson AL. Continuum theory of ductile rupture by void nucleation and growth. Part I. Yield criteria and flow rules for porous ductile media. J Eng Mater Tech 1977;99:2–15.

[16] Tvergaard V. Material failure by void growth to coalescence. Adv Appl Mech 1990;27:83–151.

[17] Garrison Jr WM, Moody NR. Ductile fracture. J Phys Chem Solids 1987;48:1035–74.

[18] Faleskog J, Shih CF. Cell model for nonlinear fracture analysis. I. Micromechanics calibration. Int J Fract 1998;89:355–73.

[19] Brazilian State Oil Company (Petrobrás). Burst pressure tests in 20. O.D. API Grade 5L X60 Pipelines. Private report; 2002 [in Portuguese].

[20] Brazilian State Oil Company (Petrobrás). Ultrasonic measurements in burst pressure tests for a 20. O.D. API Grade 5L X60 Pipelines. Private report; 2002 [in Portuguese].

[21] Brazilian State Oil Company (Petrobrás). Tensile tests for an API grade 5L X60 pipeline steel. Private report; 2002 [in Portuguese].

[22] American Petroleum Institute. API specification for line pipe. API 5L; 2000.

[23] American Society for Testing and Materials. Standard test methods and definitions for mechanical testing of steel products. ASTM A370; 2000.

[24] Silva MS. Fracture toughness and *R*-curve measurements for an API X60 pipeline steel using a direct current potential technique. MSc Thesis. Faculty of Engineering (COPPE), Federal University of Rio de Janeiro; 2002 [in Portuguese].

[25] Koppenhoefer K, Gullerud A, Ruggieri C, Dodds R, Healy B. WARP3D: dynamic nonlinear analysis of solids using a preconditioned conjugate gradient software architecture. Structural research series (SRS) 596. UILU-ENG-94-2017, Urbana-Champaign: University of Illinois; 1994.

[26] Moran B, Shih CF. A general treatment of crack tip contour integrals. Int J Fract 1987;(35):295–310.

[27] Ruggieri C, Dodds RH. Probabilistic modeling of brittle fracture including 3-D effects on constraint loss and ductile tearing. J Phys 1996.